Upscaling high activity oxygen evolution catalysts based on CoFe2O4 nanoparticles supported on nickel foam for power-to-gas electrochemical conversion with energy efficiencies above 80%

Félix Urbain[a], *Ruifeng Du*[a*], *Pengyi Tang*[a,b], *Vladimir Smirnov*[c], *Teresa Andreu*[a,d], *Friedhelm Finger*[c], *Jordi Arbiol*[b,d], *Andreu Cabot*[a,e], *and Joan Ramon Morante*[a,f]

[a] IREC, Catalonia Institute for Energy Research, Jardins de les Dones de Negre 1, 08930 Sant Adrià de Besòs, Barcelona, Catalonia, Spain

[b] Catalan Institute of Nanoscience and Nanotechnology (ICN2), CSIC and BIST, Campus UAB, Bellaterra, 08193 Barcelona, Catalonia, Spain

[c] IEK-5 Photovoltaik, Forschungszentrum Jülich, D-52425, Jülich, Germany

[d] Universitat Politècnica de Catalunya, Jordi Girona 1–3, 08034 Barcelona, Catalonia, Spain

[e] ICREA, Pg. Lluís Companys 23, 08010 Barcelona, Catalonia, Spain

[f] Universitat de Barcelona, Martí i Franquès, 1, 08028 Barcelona, Catalonia, Spain

[*] **Corresponding Author**: E-Mail: ruifengdu@irec.cat

Keywords: CoFe2O4； colloidal； OER； solar fuels ； prototype

Abstract

We investigate cobalt ferrite nanoparticles (NPs) supported on large-scale electrodes as oxygen evolution reaction (OER) catalysts. Colloidal $CoFe_2O_4$ NPs were loaded on low-cost and high surface area nickel foam (NF) scaffolds. The coating process was optimized for large electrode areas, ensuring a proper distribution of the NPs on the NF that allowed overcoming the electrical conductivity limitations of oxide NPs. We were able to produce $CoFe_2O_4$-coated NFs having 10 cm^2 geometric surface areas with overpotentials below 300 mV for the OER at a current density of 50 mA/cm^2. Such impressively low overpotentials suggested using $CoFe_2O_4$ NP-based electrodes within a water electrolysis device. In this prototype device, stable operating currents up to 500 mA at remarkably low cell-voltages of 1.62 and 1.53 V, at ambient and 50 ºC electrolyte temperatures, respectively, were reached during operation periods of up to 50 hours. The high electrochemical energy efficiencies reached at 50 mA/cm^2, 75 % and 83 % respectively, rendered these devices particularly appealing to be combined with low-cost photovoltaic systems for bias-free hydrogen production. Therefore, $CoFe_2O_4$ NP-based electrolysers were coupled to low-cost thin-film silicon solar cells with 13% efficiency to complete a system that afforded solar-to-fuel efficiencies above 10%.

1. Introduction

The development of cost-effective large-scale electrodes for highly active and stable oxygen evolution reaction (OER) catalysis is an essential step toward reaching commercial viable solutions for electrochemical water and CO_2 reduction.[1] The OER is a complex multi-step reaction that starts with an OH coordination or H_2O dissociation step in basic or acidic electrolytes, respectively, to form OH*, where (*) represents an active site at the surface of the catalyst.[2] OH* is subsequently decomposed to O*, which reacts with another adsorbed H_2O/OH to form OOH*. In a last step OOH* is deprotonated to O_2, which is finally released. This complex reaction is kinetically less favored than the concomitant hydrogen evolution reaction (HER), mainly due to the demanding formation of oxygen double bonds and the associated multi-electron transfer step. Due to its complexity, few catalysts have demonstrated high enough OER activities for commercially relevant application. Commercial electrolysis systems currently rely on expensive and scarce elements such as iridium and ruthenium,[3] since alternative low-cost catalysts suffer from unpractical high overpotential losses to provide high enough currents (> 200 mA), what makes them not competitive with alternative H_2 production pathways.[4-6]

In recent years, potentially cost-effective catalysts based on transition metal oxides not relying on Pt-group metals have demonstrated high current water electrolysis at operation voltages below 1.6 V.[7,8] However, most of these studies have been limited to small-scale electrodes or have relied on costly and energy-intensive deposition methods. These studies consequently lack of the scalability feature, which is crucial for commercial application. Against this backdrop, the present study is dedicated toward the realization of a prototype electrolyser utilizing a potentially low-cost, scalable and high throughput process for the realization of high-performing and environmentally friendly OER catalysts on large-scale electrode scaffolds.

Among non-noble OER catalysts, some spinel-type binary transition metal oxides (AB_2O_4, A, B = metal) come to the fore owing to their high abundance, low toxicity, rich redox chemistry and chemical robustness.[9-11] Besides, bimetallic catalysts offer additional degrees of freedom compared to elemental compositions, enabling further optimization of active sites towards OER catalytic steps. Among these bimetallic oxide catalysts, Co-Fe spinel compounds are a particularly interesting case of a highly abundant and potentially low-cost material that shows excellent activity toward water oxidation.[12-18]

While oxides offer high electrochemical stability, they usually suffer from intrinsically inferior electrical conductivities. To circumvent this issue and at the same time maximize the density of potential catalytic sites, oxide nano-domains need to be evenly distributed through the surface of a highly conductive scaffold that facilitates the charge transfer of the conjoint OER system. However, previous studies on $CoFe_2O_4$ particles loaded on high surface area scaffolds, such as doped carbon nanofibers [15] or hematite nanorods [19], were limited to laboratory-scale applications due to the complexity and high cost of the utilized synthesis routes and the difficulties that supporting such particles onto a large area three-dimensional (3D) scaffold involve.[13,20]

Herein, we developed a potentially low-cost, scalable, high throughput and high yield method to produce $CoFe_2O_4$ ferrite nanoparticles (NPs). Additionally, we optimized the loading of the active NPs on large-scale Ni foams (NFs), as highly conductive, 3D and cost-effective electrode scaffold. Following the optimization of the loading process and

the loaded amount of NPs, electrodes based on NFs coated with $CoFe_2O_4$ NPs were tested in a three-electrode set-up, as well as in a scaled-up two-electrode prototype electrolysis system to assess their viability for high yield H_2 production. We provide evidence that the used strategy bears great benefits regarding scalable preparation of high surface area and high activity catalysts. Additionally, we demonstrate the distribution and loading of oxide NPs to have a strong influence on the OER performance. Furthermore, we assessed the versatility of the presented system to be combined with renewable power sources by coupling the electrolyzer to a thin-film silicon solar cell for bias-free solar water splitting. Overall, the presented results set a new benchmark performance for transition metal oxides anchored on large-scale electrode support for the OER. These results will contribute to push the frontier of the field of environmentally friendly processes and electrodes for commercially viable water electrolysis,[21] electrochemical alcohol oxidation,[22] waste water treatment,[23] or nitrate reduction systems.[24]

2. Experimental Section

2.1 Chemicals and Materials

Cobalt(II) acetylacetonate ($Co(acac)_2$, 97%, Sigma-Aldrich), Iron acetylacetonate ($Fe(acac)_3$, 97% Sigma-Aldrich), oleylamine (OAm, 80–90%, TCI), oleic acid (OAc, Sigma-Aldrich), Nafion (10 wt%, perfluorinated ion-exchange resin, dispersion in water), methanol (anhydrous, 99.8%, Sigma-Aldrich), carbon black (CB, VULCAN XC72), potassium hydroxide (KOH, 85%, Sigma-Aldrich), tetrafluoroboric acid (HBF_4,48% Gew in H_2O Sigma-Aldrich) and acetonitrile (CH3CN, extra dry, Fisher) were used as received without any further treatment. Chloroform, hexane, acetone, and ethanol were of analytical grade and purchased from various sources. Milli-Q water was obtained from a PURELAB flex from ELGA. An argon-filled glove box was used for storing and handling sensitive chemicals.

2.2 *Synthesis of Colloidal $CoFe_2O_4$ Nanoparticles*

All the syntheses were performed using standard airless techniques, i.e. a vacuum/dry argon gas Schlenk line. $CoFe_2O_4$ NPs were synthesized by loading 1.0 mmol of Fe(acac)3, 1mmol of Co(acac)2, 10 ml OAm and 1.0 ml OAc in a three-neck flask and degassed under vacuum at 80 ºC for 1 hour while being strongly stirred using a magnetic bar. Subsequently, the reaction flask was heated to 230 ºC and maintained for 30 min, while continuously adding nitrogen into the flask. A visible color change was observed immediately (see Figure 1a). The obtained NPs were collected by centrifuging and washing the solid product with acetone and hexane three times. The as-prepared NPs were finally dispersed in hexane with a concentration of 10 mg/mL and stored for further use. NPs were colloidally stable in chloroform for a couple of weeks.

2.3 Ligand Removal

In a typical process, 10 mL of $CoFe_2O_4$ NPs dispersion in hexane (10mg/mL) was combined with 10 mL acetonitrile to form a two-phase mixture and then a 1 mL HBF4 solution (48%) was added. The resulting solution was sonicated until the NPs transferred from the upper to the bottom layer. The surface modified NPs were washed

with ethanol for three times and dispersed in 10 mL ethanol with a small amount of DMF for further use.

2.4 Coating of Ni Foam

Drop casting:
Ni foam was sonicated in acetone, 1M HCl, Milli-Q water, and ethanol respectively. 50 µL of 10mg/mL $CoFe_2O_4$ ethanol solution was dropped on nickel foam and dried in air and subsequently annealed at 400℃ under nitrogen atmosphere.
Dip coating:
Ni foam was sonicated in acetone, 1M HCl, Milli-Q water, and ethanol respectively. In a typical process, clean and dry nickel foam was immersed in 10mg/mL of $CoFe_2O_4$ ethanol solution for 2 seconds and then taken out quickly and dried in air. This process was repeated for 1, 3, 5, and 7times and donated as 1dip, 3 dips, 5 dips, 7dips, respectively. The coated NFs were subsequently annealed at 400℃ under nitrogen atmosphere.

2.5 Characterization

Structural characterization was carried out by X-ray diffraction (XRD). The samples were scanned from $2\theta = 20°$ to 80° at a rate of 0.02 s^{-1} in Bragg–Brentano geometry. The diffractometer was equipped with a Cu Kα (1.54051 Å) radiation source. The morphology of the as deposited foam-based electrodes was observed using a scanning electron microscope (SEM) and elemental analysis was performed by the same microscope equipped with an X-ray energy dispersive spectrometer (EDS). The samples for transmission electron microscope (TEM) were prepared by scratching the as-prepared $CoFe_2O_4$ powders from the Ni foam substrate, followed by dispersing them in hexane and collecting them on the TEM copper grids. High resolution transmission electron microscopy (HRTEM) images and scanning transmission electron microscopy (STEM) studies were conducted by using an FEI Tecnai F20 field emission gun microscope operated at 200 kV with a point-to-point resolution of 0.19 nm, which is equipped with high angle annular dark field (HAADF) and electron energy loss spectroscopy (EELS) detectors.
The electrochemical performance of $CoFe_2O_4$@NF electrodes towards OER reduction was assessed using a three-electrode set-up. A leak-free Ag/AgCl 3.4 M KCl reference electrode (RE) was assembled in the polytetrafluoroethylene (PTFE) frame of the cell and placed very close to the working electrode surface. The potential was transformed to the reversible hydrogen electrode (RHE) scale: $E\ (V_{RHE}) = E\ (V_{Ag/AgCl}) + 0.0592 \times pH + 0.197$. The data presented for the electrochemical characterization in aqueous solutions in three-electrode configuration do not include compensation for the series resistance of the solution. For the complete electrolyzer characterization, an adapted flow cell set-up (Micro Flow Cell, Electrocell A/S) was employed, schematically depicted in Figure 7a. The flow rates of electrolytes within the flow cell were kept at 20 ml/min. As illustrated in Figure 7a, the electrolyte was directly introduced through the macroporous 3D $CoFe_2O_4$@NF electrode (geometric surface area: 10 cm^2). For details on the cyclic voltammetry (CV) and gas chromatography (GC) regarding the assessment of current-voltage behavior and the faradaic efficiency for gaseous products, respectively, the reader is referred to Ref. 33 and Ref. 34. The electrically attached triple junction thin-film silicon device had an area of 1 cm^2, thus during the photoelectrolysis measurement an area of 1 cm^2 was illuminated. All photoelectrochemical experiments were

conducted using a solar simulator equipped with a 150 W xenon lamp. The intensity of the light source was adjusted to match standard AM 1.5G sunlight at 100 mW/cm^2 intensity. The experiments for the full system assembly were carried out in a two-electrode configuration. The faradaic efficiency to H_2 was calculated using the analysis of the outlet gas by gas chromatography (GC) during potentiostatic measurements. Helium (99.999%) was used as the carrier gas. The calibration of peak area vs. gas concentration was used for the molar quantification of each gaseous effluent. The faradaic efficiency was calculated by determining the number of coulombs needed for each product and then dividing by the total charge passed during the time of the GC sampling according to the flow rate. In the photovoltaic-electrolyzer coupled system, to account for deviations in the assessment of the photovoltaic performance of the complete system, i.e. spectra variations due to diode calibration accuracy, area definition, or temperature variation, a systematic error of 2 % was considered.[39]

3. Results and discussion

3.1 Synthesis and Characterization of Colloidal $CoFe_2O_4$ NPs

Co-Fe oxide NPs were produced in colloidal form from the reduction of cobalt and iron salts in the presence of OAm and OAc and the posterior oxidation of the reaction product in ambient conditions (Scheme 1, see Experimental Section for details). A representative transmission electron microscopy (TEM) micrograph and the size distribution histogram of the oxidized NPs are shown in Figure 1a. Co-Fe oxide NPs displayed a quasi-spherical geometry, with an average diameter of 7.1 ± 0.1 nm. In contrast to the product of the oxidation of iron NPs, the oxidation of Co-Fe NPs did not result in the formation of hollow structures, probably due to the relatively low diffusivity of Fe and Co through the growing Co-Fe oxide shell compared with that of Fe though $FeO/_g$-Fe_2O_3.[25-27]

X-ray diffraction (XRD) analysis revealed Co-Fe oxide NPs to crystallize in the $CoFe_2O_4$ cubic phase (JCPDS *22-1086,* Figure 1b). High resolution TEM (HRTEM) micrographs confirmed the crystal structure of the NPs to be compatible with the $CoFe_2O_4$ ferrite cubic phase ([FM3-MZ]-Space group 227) with lattice parameters a = b = c = 0.83961 nm (Figure 2b). Annular dark-field scanning TEM micrographs (ADF-STEM) and electron energy loss spectroscopy (EELS) analysis demonstrated the three constituent elements, Co, Fe, and O, to be present in the same ratio in all NPs and to be homogeneously distributed within each NP (Figure 2a).

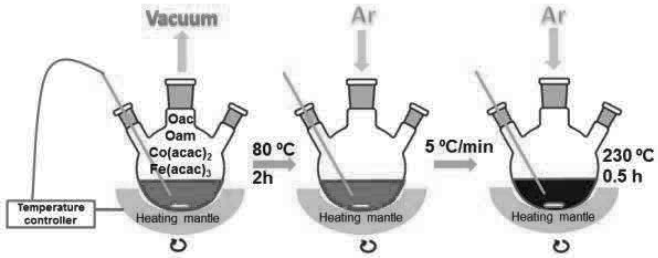

Scheme 1. Schematic illustration of the synthesis procedure used to prepare colloidal $CoFe_2O_4$ NPs.

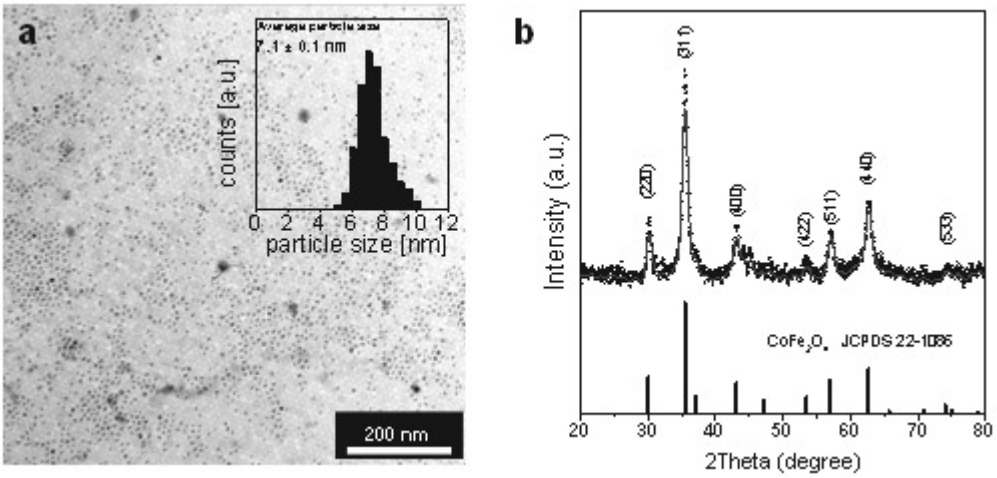

Figure 1. a) Representative TEM micrograph of as-prepared $CoFe_2O_4$ NPs. Inset displays the corresponding size distribution histogram from where an average NP diameter of 7.1 ± 0.1 nm was estimated. b) XRD pattern of the as-prepared $CoFe_2O_4$ NPs. Graph includes the reference pattern JCPDS 22-1086 for the cubic $CoFe_2O_4$ crystal phase.

X-ray diffraction (XRD) analysis revealed Co-Fe oxide NPs to crystallize in the $CoFe_2O_4$ cubic phase (JCPDS *22-1086,* Figure 1b). Annular dark-field scanning TEM micrographs (ADF-STEM) and electron energy loss spectroscopy (EELS) analysis demonstrated the three constituent elements, Co, Fe, and O, to be present in the same ratio in all NPs and to be homogeneously distributed within each NP (Figure 2a). High resolution TEM (HRTEM) micrograph confirmed the crystal structure of the NPs to be compatible with that of the $CoFe_2O_4$ ferrite cubic phase (Fd-3m Space group 227) with lattice parameters of a = b = c = 0.83961 nm (Figures 2b and S1).

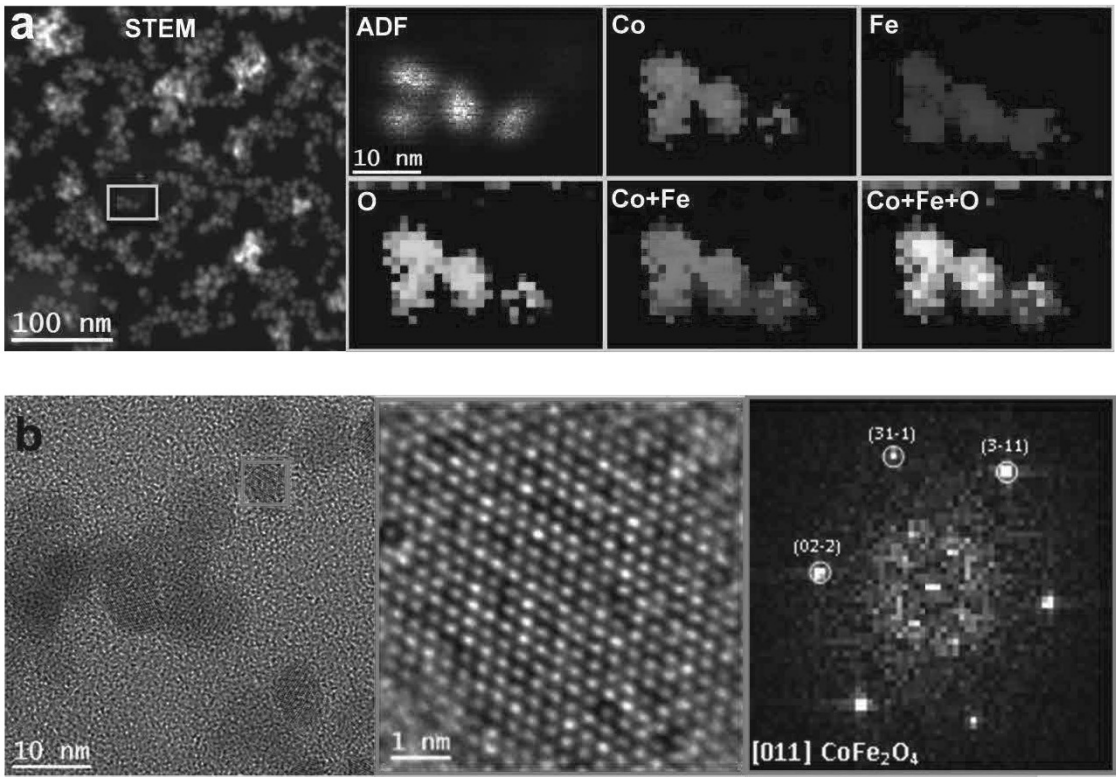

Figure 2. a) ADF-STEM micrograph and EELS chemical composition maps (from cyan rectangle) for Co (red), Fe (blue), O (green) and their composites. b) HRTEM micrograph, detail of the red squared region (scale bar, 1 nm), and corresponding FFT spectrum indicating that NPs crystallized in the cubic $CoFe_2O_4$ phase, [FM3-MZ]-Space group 227, with lattice parameters of a = b = c = 0.83961 nm, and $\alpha = \beta = \gamma = 90°$ as visualized along the [011] direction.

N_2 adsorption–desorption isotherms of the $CoFe_2O_4$ NPs dried in the form of a powder displayed a type-I reversible behavior (Figure 3), which generally a signature of microporous solids.[28] $CoFe_2O_4$ nanopowders were characterized by a Langmuir specific surface area (SSA) of 276 m^2/g and a Brunauer–Emmett–Teller (BET) SSA of 174 m^2/g. The obtained BET SSA is among the highest reported for Co-Fe spinel NPs, slightly above that of NPs synthesized by hydrothermal[13] and micro emulsion techniques[20] (~150 m^2/g), and significantly higher than materials prepared by electrospinning[15] and electrodeposition[16] (~55 m^2/g). Notice that these high SSAs were measured from the nanopowders obtained by drying the colloidal NPs in ambient conditions and with no pre-coordination of the NP into a network. Even larger SSA values would be potentially obtained through the formation of NP networks in solution, i.e. NP gelation, and the posterior drying from supercritical CO_2 for instance.[29,30]

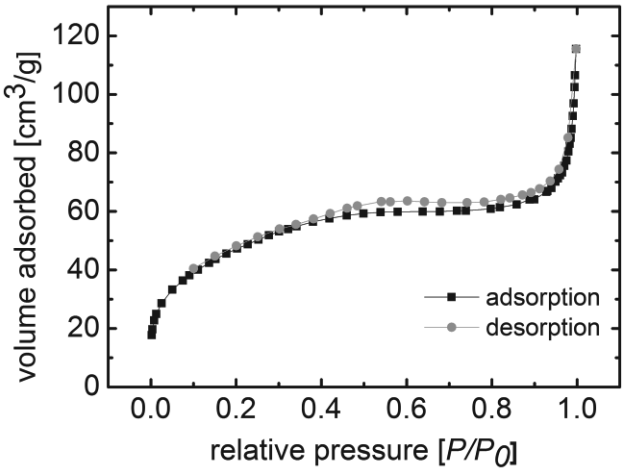

Figure 3. N_2 adsorption–desorption isotherms from the $CoFe_2O_4$ nanopowders obtained from drying $CoFe_2O_4$ NPs under ambient conditions

3.2 Loading on Large-scale Ni Foams

The optimized loading of nano-sized OER catalysts onto large-scale scaffolds is an important step toward the realization of industry-viable electrodes and electrolyzers. In this direction, we first studied the deposition of NPs on small (1 cm^2) NF electrodes and subsequently optimized the deposition process for larger scaffolds (≥ 10 cm^2). Before deposition, organic ligands at the surface of as-synthesized NPs, which were used to adjust NP growth during the synthesis, were removed using a solution of tetrafluoroboric acid in acetonitrile (see Experimental Section). After successive cleaning with tetrafluoroboric acid, Fourier transform infrared (FTIR) spectra showed the disappearance of the peaks at 2822 and 2890 cm^{-1} corresponding to C–H stretching modes, what evidenced the effective removal of hydrocarbon ligands (Figure S3). This ligand displacement step is key towards producing high performance and reliable electrocatalyts since generally organic ligands strongly limit electronic transport and the ability of the NPs to interact with their surrounding media, i.e. with the scaffold and the electrolyte.[31] Furthermore, in the present case, the presence of organic ligands on the surface of the $CoFe_2O_4$ NPs particularly impeded a homogeneous coating of the NF. Not mediating a ligand removal pretreatment, a porous two-dimensional organic film was deposited on the NF after dip coating it into a suspension of colloidal NPs (Figure S2).

Two procedures were explored to support $CoFe_2O_4$ NPs on NFs: dip coating and drop casting. As depicted in figure 4a, the foam was either dipped into the dispersion of colloidal NPs and hold for 2 seconds or the suspension was dropped onto the foam (2 mg of solution) and let it dry. SEM characterization showed the dip coating process to result in a homogeneous distribution of NPs on the NF surface. On the other hand, drop-casted NFs displayed numerous NP agglomerates.

The electrochemical performance toward OER of NFs loaded with $CoFe_2O_4$ NPs (hereafter $CoFe_2O_4$@NF) is shown in Figure 4b. In comparison with bare NF, used in industrial water splitting, $CoFe_2O_4$@NF electrodes displayed significantly enhanced OER catalytic activities. $CoFe_2O_4$@NF electrodes provided much higher current

densities under the same applied potential than bare NF (Figure 4c). In addition, $CoFe_2O_4$@NF electrodes prepared by dip coating provided higher performance over electrodes prepared by drop casting. This result was consistent with the usual assumption that thinly dispersed oxide nanoparticles favor electrochemical performance.[32] A significant increase in the current density for potentials > 1.5 V was measured for samples prepared by dip coating, attaining 43.8 mA/cm^2 at 1.7 V_{RHE} (470 mV overpotential), which is 1.4 times higher than the current density obtained with the drop casted sample (Figure 4b).

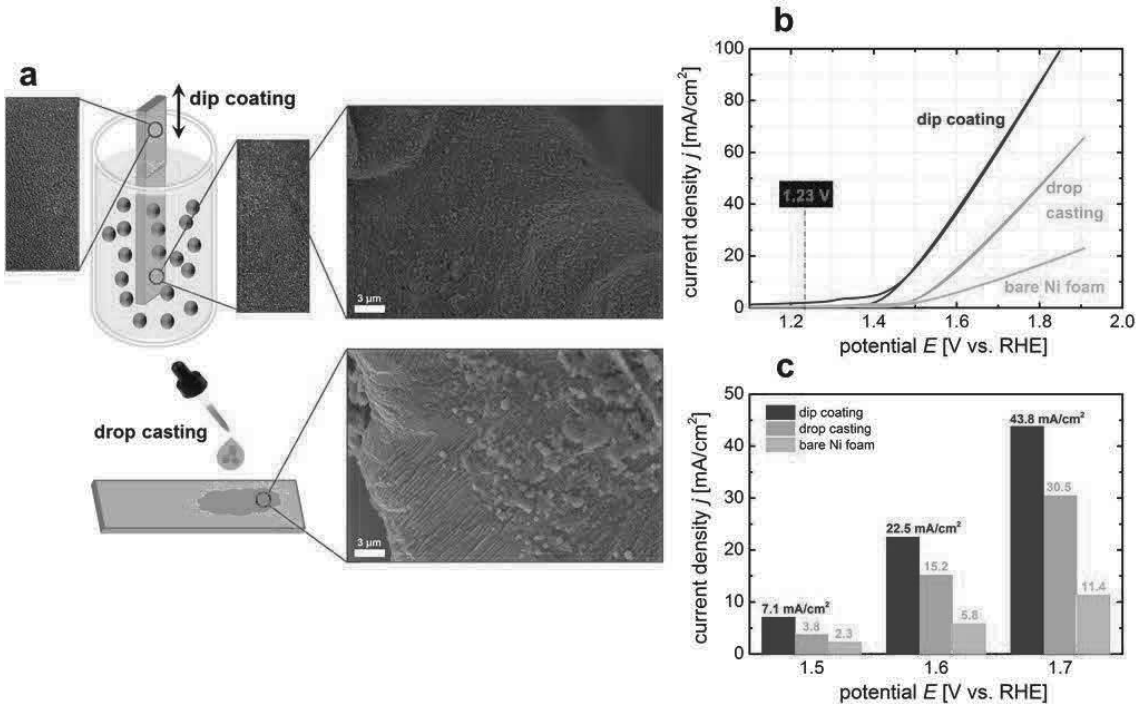

Figure 4. a) Schematic illustration of the two tested coating techniques for the $CoFe_2O_4$ NPs on the NF (1 cm^2 geometric area): dip coating and drop-casting, including photographs of the NF before and after the coating processes, as well as SEM images showing the distribution of the deposited NPs on the NF. b) CV curves of the NF coated with $CoFe_2O_4$ NPs by dip coating and drop casting, respectively, compared with bare NF. Measurements were conducted in 1 M KOH at a scan rate of 10 mV/s. c) Current densities achieved at different applied potentials.

The dip coating technique was further optimized for large area electrodes (10 cm^2). Figure 5 presents SEM images of the NF surfaces after 1, 3, 5, and 7 dips (each hold for 2 seconds) into the $CoFe_2O_4$ NP suspension. After 1 dip, major parts of the NF remained uncovered, whereas 3 dips resulted in a high coverage of the NF surface with highly dispersed NPs (Figure S4). Increasing the number of dips to 5 led to the formation of NP aggregates with sizes ranging from 50 to 200 nm (Figure 5). This effect was even more pronounced after 7 dipping times, resulting in an almost complete coverage of the NF surface by $CoFe_2O_4$ NP agglomerates.

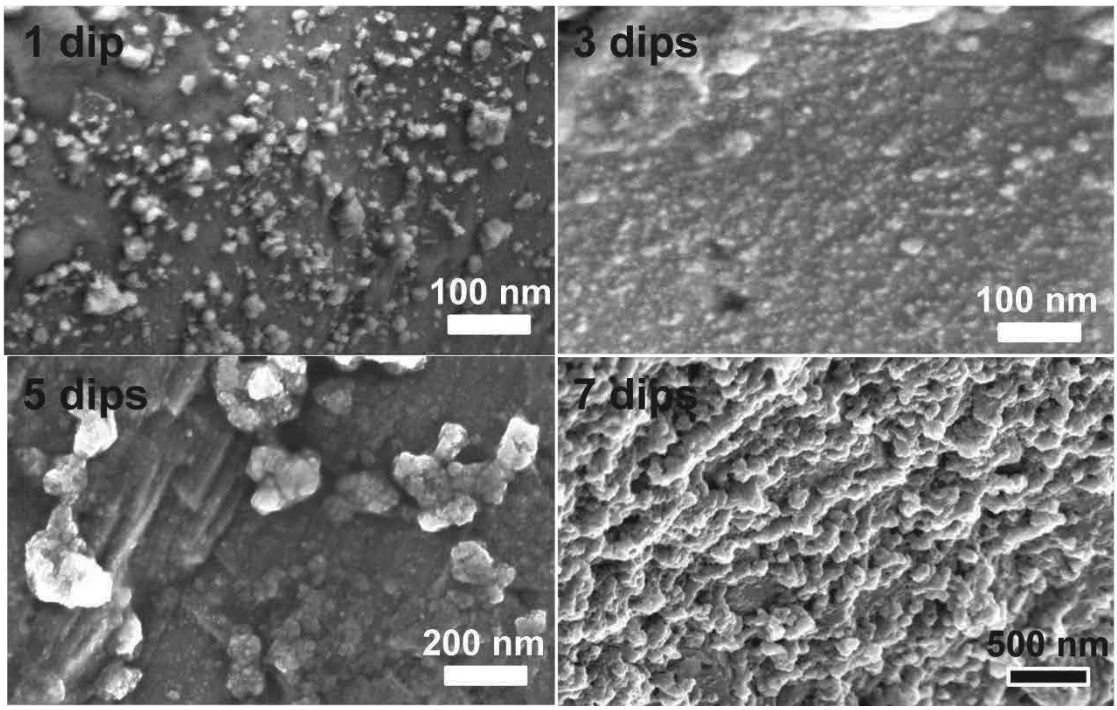

Figure 5. SEM micrographs of $CoFe_2O_4$@NF electrodes (10 cm^2) produced using different dip coating steps:1, 3, 5, and 7 as noted in each micrograph.

The electrochemical characteristics of the large-scale $CoFe_2O_4$@NF electrodes were assessed in a three-electrode configuration using 1M KOH electrolyte solution (see Experimental Section). Figure 6a shows the CV curves of the electrode samples investigated in Figure 5. The number of dip coating steps had a significant influence on the OER performance. Best performances were achieved with $CoFe_2O_4$@NF electrodes produced using 3 dip coating steps, in good agreement with the observed homogeneous coverage of the NF surface with thinly dispersed NPs. OER overpotentials of the four tested samples for different current densities are shown in Figure 6b. $CoFe_2O_4$@NF electrodes produced after 3 coating steps exhibited the lowest overpotentials, with 250 mV and 460 mV for 10 mA/cm^2 and 50 mA/cm^2, respectively. Higher $CoFe_2O_4$ NP loads containing NP agglomeration provided lower OER performance. This result is understandable as oxide structures generally suffer from low electrical conductivities, which strongly limits the thickness of the oxide layer that can be practically used. The highest overpotential of 580 mV at 50 mA/cm^2 was measured for the 1 step coating $CoFe_2O_4$@NF electrode, presumably due to an insufficient coverage of the scaffold with $CoFe_2O_4$ NPs (Figure 5).

Commercial alkaline electrolyzers work at operating temperature between 25 and 100 ^oC, which is why we tested the best performing electrode (3 dips) also under elevated electrolyte temperature. As observed in Figure 6a and 6b, the OER performance was significantly enhanced by increasing the electrolyte temperature up to 50 ^oC, mainly due to enhanced electrochemical kinetics. Extremely low overpotentials of 200 mV and 295 mV for 10 mA/cm^2 and 50 mA/cm^2, respectively, were obtained. Such values are among the best state-of-the-art OER electrodes in literature, evidencing the high potential for commercial applications of the herein developed large-scale $CoFe_2O_4$@NF OER electrodes. State-of-the-art electrocatalytic properties toward OER of previously reported Co-Fe or NF based electrodes are summarized in Table S1 in the SI.

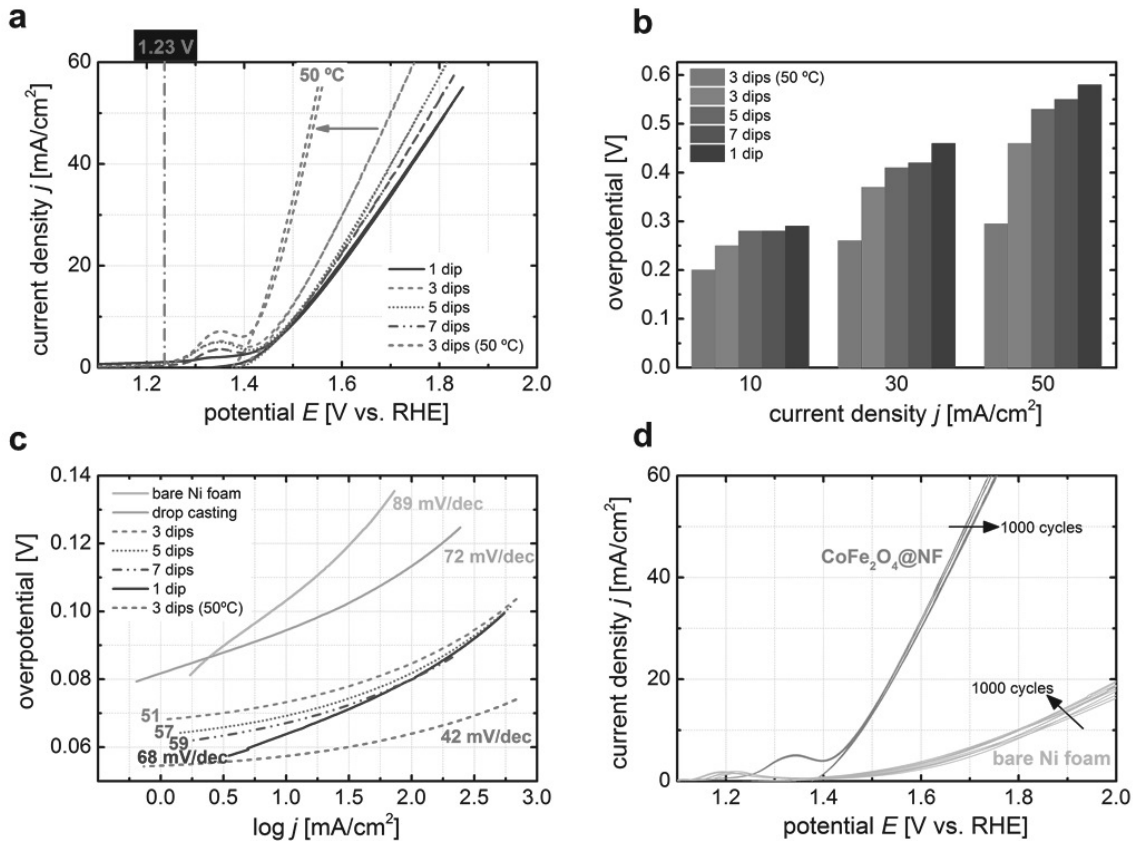

Figure 6. a) CV curves of NF electrodes dipped into the $CoFe_2O_4$ NP solution, for 1 (solid), 3 (dashed), 5 (dotted), and 7 (dash-dotted) times. CV curves were measured in 1M KOH at a scan rate of 10 mV/s. $CoFe_2O_4$@NF electrodes providing best OER catalytic performances (3 dips) were measured under elevated electrolyte temperature (50 ºC, pink dashed line). The H_2O/O_2 oxidation potential is indicated by the straight dash-dotted line. b) Required overpotentials derived from CV curves at different current densities. c) Tafel plots of the tested samples. d) CV curves of the $CoFe_2O_4$@NF (3 dips) and bare NF electrodes, respectively, before and after 1000 cycles. Every 200th CV scan of each electrode is plotted.

The electrocatalytic kinetics for OER of the $CoFe_2O_4$@NF electrodes were further investigated by Tafel plots (Figure 6c). For comparison, the Tafel plots of the sample prepared by drop casting and the bare NF sample are also shown in Figure 6c. In accordance with the results shown in Figure 4b and 4c, the drop casted and the bare NF electrodes exhibited the worst kinetics among the analyzed electrodes, i.e. the highest Tafel slopes, at 89 mV/dec and 72 mV/dec, respectively. For the $CoFe_2O_4$@NF electrodes prepared by dip coating, Tafel slopes were impressively low and ranged from 68 mV/dec for the 1 time dipped sample to 51 mV/dec for the 3 times dipped electrode. Hence, our $CoFe_2O_4$@NF electrodes showed comparable and even better electrocatalytic properties toward OER than related nonprecious metal-based OER electrocatalysts reported in literature (Table S1 of the SI). The $CoFe_2O_4$@NF electrode measured in a 50 ºC alkaline solution provided the lowest Tafel slope, 42 mV/dec, as could be expected from the corresponding CV curve in Figure 6a. In fact, such an outstanding kinetic behavior made it an ideal anode candidate for commercial electrolysis systems.

Besides electrochemical performance, durability is another major parameter in the realization of industry-viable electrodes for electrolyzers. In this direction, we investigated the long-term stability for $CoFe_2O_4$@NF electrodes (3 dips) by cycling them 1000 times in 1M KOH at ambient temperature (Figure 6d). Again, bare NF was utilized for comparison. $CoFe_2O_4$@NF electrodes showed a negligible degradation after continuous 1000 CV cycles, indicating its superior operational stability under alkaline test condition. This was also confirmed by HRTEM analysis of the used catalyst, showing the $CoFe_2O_4$ NPs to remain thinly dispersed onto the NF and maintaining their size after the long-term experiment (Figure S5). No obvious NP aggregation/growth was observed, which was associated to the proper immobilization of the $CoFe_2O_4$ NP on the NF. Consistently with previous reports, bare NF slightly increased its activity towards OER with time (Figure 6d). In alkaline solution, this activity enhancement has been associated to the contribution to the catalytic activity of metallic impurities (e.g. Fe) from the electrolyte that are deposited onto the Ni surface during long-term operation.[33] Because such a behavior was not observed with $CoFe_2O_4$@NF electrodes, we assume that the Ni scaffold have a moderate catalytic role in this system.

We estimated the electrochemical active surface area (ECSA) of $CoFe_2O_4$@NF (3 dips) and bare NF electrodes from the electrochemical double-layer capacitance (C_{dl}) at the solid/liquid interface.[34] Figure S6a and S6b (SI) present the CV curves of the two electrodes recorded in a non-Faradic potential range under different scan rates. $CoFe_2O_4$@NF cathodes exhibited a higher C_{dl} than bare NF, evidencing a higher active surface area, which was estimated as 80.5 cm^2 for $CoFe_2O_4$@NF and 31.0 cm^2 for bare NF (Figure 6c). This result probes the $CoFe_2O_4$@NF to provide a larger number of catalytically active sites and thus an improved OER activity, much higher than that of $CoFe_2O_4$ NPs on carbon nanofibers (20.6 cm^2) and commercial RuO_2 catalyst (14.5 cm^2).[15]

3.3 Prototype Electrolysis Reactor

The optimized large-scale $CoFe_2O_4$@NF electrode was subsequently integrated in a prototype electrolysis reactor.[35-37] As illustrated in Figure 7a, the reactor design allowed to work under flow conditions, where the anolyte and catholyte solutions are continuously recirculated through the respective compartments, i.e. a $CoFe_2O_4$@NF anode compartment performing the OER and a Ti/Pt cathode compartment performing the hydrogen evolution reaction (HER). By this design, the flow dynamics of the electrolysis set-up could be significantly enhanced, fostering higher electrochemical activity. Both compartments were separated by a membrane and a gas chromatograph was employed for gaseous product identification. The configuration can even be adapted for the additional integration of photovoltaic devices, as shown in Figure 7a with a thin-film silicon solar cell (see Experimental Section for details).

The characteristics of the complete reactor in two-electrode operation are shown in Figure 7b for two different configurations. The first configuration consisted in using a cation-exchange membrane (Nafion ®117) and 1M KOH electrolyte solution in both compartments. In the second configuration, we applied a bipolar membrane (BPM), enabling to operate the electrolysis reactor with two different electrolytes. In this configuration, we applied a 1M KOH (pH = 13.7) for the anolyte to perform the OER and a 1M H_2SO_4 (pH = 0) solution for the catholyte to perform the HER. As can be seen from the linear sweep voltammetry (LSV) curves in Figure 7b, the configuration using the BPM exhibited a better overall electrolysis behavior than the reactor configuration

containing the Nafion membrane. To provide 200 mA and 400 mA, respectively, the BPM configuration only required 1.51 V and 1.59 V, respectively, whereas in the Nafion configuration the complete electrolyser cell voltage augmented to 1.60 V and 1.76 V, respectively. The higher cell voltage was related with the reduced electrochemical performance of the Ti/Pt cathode in alkaline solution (Nafion configuration) compared to its performance in acid electrolytes (BPM configuration). In Figure S7, the LSV curves of Ti/Pt in 1M KOH and 1M H_2SO_4 electrolyte solution are shown. LSV curves displayed overpotentials of 340 mV and 180 mV at 50 mA/cm^2 for basic and acidic catholytes, respectively, further demonstrating the superior cathode performance in acidic medium. To simulate real electrolyser conditions, the overall polarization of the reactor device was also measured at elevated electrolyte temperatures (50 ºC) in the BPM configuration. As expected from the results shown in Figure 6a and Figure S7, the electrochemical performance increased with increasing electrolyte temperature, reaching complete electrolyzer cell voltages of 1.46 V and 1.51 V to produce 200 mA and 400 mA, respectively. From these values, electrochemical energy efficiency up to 75 % and 83 %, for ambient and elevated operation temperatures were calculated. Consequently, the herein proposed electrolyzer based on a $CoFe_2O_4$@NF electrode presents an attractive alternative to commercial systems used for surplus electric power storage, such as pumped hydroelectric storage (70–80% efficiency), power-to-gas based on alkaline and PEM electrolyzers (65–70% efficiency), or ion lithium batteries (92–95% efficiency) that have other severe limitation in terms of energy density, cost and life time.

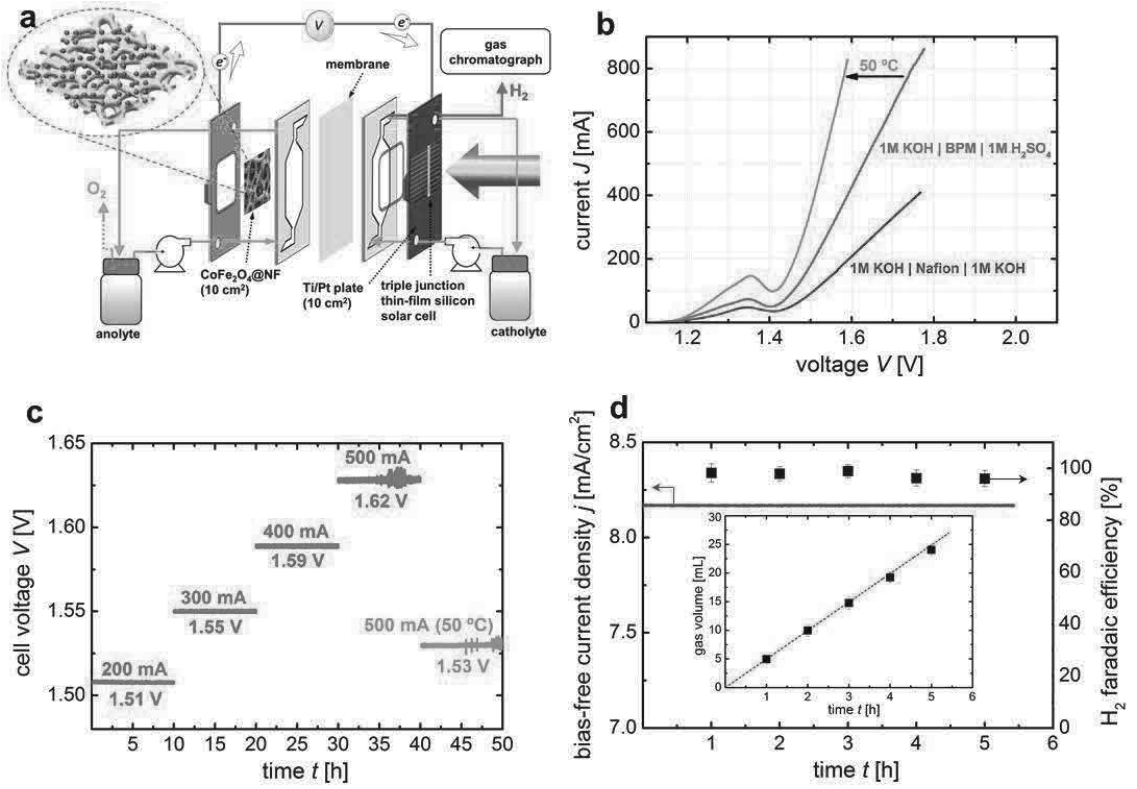

Figure 7. a) Sketch of the experimental prototype reactor used to assess the overall electrolysis performance. The illustration shows the different components, including a schematic illustration of the 3D NF coated with $CoFe_2O_4$ NPs and the coupled triple junction thin-film silicon solar cell (a-Si:H/a-Si:H/µc-Si:H) for the bias-free operation test (see Figure 7d). b) Linear sweep measurements of the $CoFe_2O_4$@NF electrodes (10 cm^2 geometric area) combined with the Ti/Pt

cathode (10 cm^2 geometric area) for a configuration containing Nafion and BPM membrane, respectively. The BPM configuration (best performing) was also measured at 50 ºC electrolyte solution (1M KOH). c) Long-term behavior of the electrolysis showing the required cell voltages of the reactor as a function of the applied current (each galvanostatic testing was conducted for ~10 hours with the same electrodes and membrane). d) Bias-free solar water splitting using a triple junction a-Si:H/a-Si:H/µc-Si:H solar cell (as depicted in a)). Left y-axis shows the achieved bias-free current density over the operation time. Right y-axis represents the faradaic efficiency for H_2 production over the operation time. The error bars indicate standard deviations obtained from 3 experimental repeats. The inset shows the calculated gas volume obtained. The dotted purple line shows the theoretical (assuming 100% faradaic efficiency) gas evolution for the measured bias-free current density and the black squares show the experimental values.

The electrochemical durability of the prototype reactor was assessed by conducting chronoamperometry. Figure 7c displays the electrolyzer cell voltages at successively increasing electrolysis currents of 200, 300, 400, and 500 mA applied for 10 hours each, until a total of 50 hours of continuous operation. The prototype electrolyzer showed no sign of decay when operated for 50 hours, even when operated at higher temperature (50 ºC).

Given its remarkable activity and high electrochemical energy efficiency, the prototype electrolysis reactor can be effectively powered by renewable energy sources, such as photovoltaics.[21-24]. In this direction, the conversion of solar energy into chemical fuels energy is a promising route for future conversion and storage concepts. Solar-to-fuel conversion efficiencies using photovoltaics and electrolyzers depends on the efficiency of the two systems. Taking into account electrochemical conversion efficiency above 80 % as reached for $CoFe_2O_4$@NF electrodes, their combination with commercial high efficiency solar cells having 30% conversion efficiencies could result in 24 % solar-to-fuel conversion efficiencies. However, in the present work, to aachieve cost-efecivenes, we aimed at reducing the system cost using amorphous silicon solar cells. Thus, we electrically connected the prototype electrolyzer to a low-cost triple junction a-Si:H/a-Si:H/µc-Si:H solar cell with a photovoltaic conversion efficiency of around 13.4% (Figure 7a.).[38] In figure S8, the system current density-voltage *(j-V)* curve is overlaid with the polarization curve of the electrolyzer device. The crossing point of both *j-V* curves, which can serve to estimate the bias-free operation current density of the solar-driven electrolyzer, lied in the plateau region of the solar cell characteristics (near the maximum power point) at 1.45 V and 8.2 mA/cm^2. The bias-free measurement of the solar-driven electrolyzer is shown in Figure 7d. This result demonstrates that the prototype electrolyzer can be powered only by sunlight energy, providing current densities up to 8.2 ± 0.2 mA/cm^2. The faradaic efficiency for H_2 production, measured by gas chromatography, was found to be close to 100 % over the course of bias-free operation (> 5 hours), as depicted on the right ordinate in Figure 7d. The inset in Figure 7d shows the theoretical and experimentally determined bias-free H_2 gas production over time, proving that H_2 was the only product formed during electrolysis (besides O_2). With these values, a solar-to-hydrogen conversion efficiency of 10.0 ± 0.2 % was calculated, which is among the record bias-free water splitting efficiencies for thin-film silicon based devices.[38,40,41]. Overall, this example demonstrates that electrolyzers based on $CoFe_2O_4$@NF electrodes can match the stringent requirements for cost-effective renewable energy conversion and storage at large scale.

4. Discussion

The enhanced OER catalytic activity of the $CoFe_2O_4$@NF electrodes here presented can be ascribed to the combination of nano-sized active $CoFe_2O_4$ particles with the 3D macroporous structure of the supporting NF, as illustrated in Figure 7a. This marriage resulted in a significantly increased contact area between catalysts and electrolytes and provided a greater amount of active sites where OER could take place (see ECSA estimation in the SI, Figures S6c). The dip coating procedure eventually led to an optimum distribution of thinly dispersed $CoFe_2O_4$ NPs (Figure 5), which allowed to circumvent the intrinsically inferior electrical conductivity of oxide particles (see low Tafel slopes in Figure 6c), while ensuring an impressive stability of the $CoFe_2O_4$@NF electrode (Figure 6d and Figure 7c).

The large-scale electrode used, the high stability demonstrated and the low electrolyser cell voltages at industrial relevant currents and at ambient and elevated temperature probed the technology relevance of the present system. Values reported here are among the record performance indices for overall water splitting using inexpensive and earth-abundant catalysts. Additionally, the present study assessed their performance on large-scale electrodes in a prototype electrolyzer. While the aspect of process scalability is vital in view of a real-world application, it has neither been experimentally evidenced, nor sufficiently discussed in previous related studies on OER materials (exemplarily see electrode areas in Table S1 in the SI). These previous studies focused on laboratory scale electrodes, neglecting critical issues, which have been addressed in the present study, such as homogeneous coverage of active electrocatalyst on large-scale scaffolds, higher chemical resistivity or low-cost and high throughput and yield processing techniques.

In general, the coupling of pure academic with engineered systems is urgently needed to mature renewable fuel production processes and open the pathway towards commercial application. This aspect is successfully addressed by the herein proposed system. In addition, the scalable process of the developed $CoFe_2O_4$@NF electrode paired with the adaptability of the presented prototype reactor bears great benefits and cross-fertilization for a number of related catalytic and photovoltaic technologies. Thus, our electrolyzer concept is not limited to small active electrode areas[42,43] or expensive small-scale photovoltaic structures[44] but can be adapted to large scale designs. Nevertheless, from a scientific point of view, further attention should be devoted to investigate earth-abundant and active HER electrodes. The herein applied Ti/Pt plate served as stable and reliable proof-of-concept electrode, but could be replaced by a cathode system, which does not contain rare materials such as Pt. From a more engineering point of view, the evaluation of different approaches to upscale the photovoltaic structures up to the geometric size of the electrochemical active surface areas could be alluring if integrated photoelectrochemical cell (PEC) systems are envisaged. In this “PEC-farm” approach, multiple medium-scaled electrolyzers, i.e. electrolyzers similar to the herein presented prototype (10-100 cm^2 active photovoltaic and electrochemical electrode areas), could operate independently, while the produced fuels of all the electrolyzers would be collected together.[45] The advantageous feature of this concept is that lower photocurrent densities would be required, which would be beneficial regarding lower overpotential losses and thus, eventually higher overall solar-to-fuel efficiencies. In this regard, it is projected by techno-economic models of large scale, centralized solar H_2 production facilities that overpotential losses at high operating current densities are one of the most important factors in reducing the STH efficiency and thus, increasing the cost of H_2.[46,47]

In total, all these examples manifest the high versatility and cross-fertilization of the herein presented scalable $CoFe_2O_4$@NF electrode and electrolysis system, respectively.

5. Conclusion

In conclusion, we have presented a simple and scalable colloidal synthesis and coating strategy for the homogeneous anchoring of bimetallic $CoFe_2O_4$ NPs on large-scale NF. $CoFe_2O_4$@NF electrodes were demonstrated to be an efficient earth-abundant OER electrocatalysts with ultralow overpotential, large current density, small Tafel slope, and long-term durability in alkaline solution. The improved catalytic performances are believed to originate from the unique synergy between the nano-scaled active $CoFe_2O_4$ NPs and the highly conductive and high area Ni scaffold. Considering cost-effectiveness, facile, as well as reliable fabrication processes, and the outstanding catalytic performance of $CoFe_2O_4$@NFs may hold great potential in future energy conversion and storage devices. Moreover, the performance of the large-scale $CoFe_2O_4$@NF (10 cm^2 geometric active area) was investigated in a prototype electrolysis reactor, where currents of 500 mA were achieved with electrolyzer cell voltages of 1.62 V and 1.53 V at ambient and elevated temperatures, respectively, over prolonged operation times. Overall, the presented electrochemical results paired with the versatile synthetic and coating strategy may stimulate future lines of work, which will be needed to address efficiency improvements and techno-economical questions while assessing cost competitiveness of promising (photo)-electrochemical technologies.

Acknowledgments

Authors acknowledge funding from Generalitat de Catalunya through the CERCA program, 2017 SGR 1246, 2017 SGR 327 and the Spanish MINECO projects MAT2014-59961, ENE2016-80788-C5-5-R, ENE2016-77798-C4-3-R and ENE2017-85087, together with the support from Repsol S. A. Likewise, the authors thank Enagás S.A. ICN2 is supported by the Severo Ochoa program from Spanish MINECO (Grant No. SEV-2017-0706). IREC also acknowledges additional support from the European Regional Development Funds (ERDF, FEDER), (S)TEM part of the present work has been performed in the framework of Universitat Autònoma de Barcelona Materials Science PhD program and the rest in the Nanoscience program of the University of Barcelona. The authors thank S. Moll (IEK-5), M. Biset-Peiró (IREC), and H. Xie (IREC) for their contribution to this work. F.U. acknowledges financial support from MINECO through Juan de la Cierva fellowship (FJCI-2016-29147).V.S. and F.F. (authors from IEK-5) thank the Deutsche Forschungsgemeinschaft (DFG) (Priority Program SPP 1613).

Author contributions

F.U., J. R. M. and A.C. conceived the project and designed the experiments. F.U. carried out the (photo)-electrochemical experiments. R.D. conducted the synthesis and coating of the Ni foam. P.Y.T., R.D. and J.A. conducted the structural and

compositional analyses. F.U., R.D. and P.Y.T. interpreted data. F.U. wrote the manuscript. V.S. and F.F. performed and supervised the deposition of the multijunction thin-film silicon solar cells. J.R.M. T.A. and A.C. supervised the proposed and executed research program. All the authors participated in discussions and contributed to editing of the manuscript.

Conflict of Interest

The authors declare no conflict of interest.

6. References

[1] S.B. Walker, U. Mukherjee, M. Fowler, A. Elkamel, International Journal of Hydrogen Energy 41 (2016) 7717-7731.
[2] N.-T. Suen, S.-F. Hung, Q. Quan, N. Zhang, Y.-J. Xu, H.M. Chen, Chemical Society Reviews 46 (2017) 337-365.
[3] C.C. McCrory, S. Jung, I.M. Ferrer, S.M. Chatman, J.C. Peters, T.F. Jaramillo, Journal of the American Chemical Society 137 (2015) 4347-4357.
[4] S. Ardo, D.F. Rivas, M.A. Modestino, V.S. Greiving, F.F. Abdi, E.A. Llado, V. Artero, K. Ayers, C. Battaglia, J.-P. Becker, Energy & environmental science 11 (2018) 2768-2783.
[5] M. Ball, M. Weeda, International Journal of Hydrogen Energy 40 (2015) 7903-7919.
[6] T. Rostrup-Nielsen, Catalysis Today 106 (2005) 293-296.
[7] K. Chakrapani, G. Bendt, H. Hajiyani, I. Schwarzrock, T. Lunkenbein, S. Salamon, J. Landers, H. Wende, R. Schlögl, R. Pentcheva, ChemCatChem 9 (2017) 2988-2995.
[8] H. Zhou, F. Yu, Q. Zhu, J. Sun, F. Qin, L. Yu, J. Bao, Y. Yu, S. Chen, Z. Ren, Energy & Environmental Science 11 (2018) 2858-2864.
[9] T. Maiyalagan, K.A. Jarvis, S. Therese, P.J. Ferreira, A. Manthiram, Nature communications 5 (2014) 3949.
[10] M. Tahir, L. Pan, F. Idrees, X. Zhang, L. Wang, J.-J. Zou, Z.L. Wang, Nano Energy 37 (2017) 136-157.
[11] M. Li, Y. Xiong, X. Liu, X. Bo, Y. Zhang, C. Han, L. Guo, Nanoscale 7 (2015) 8920-8930.
[12] A. Kargar, S. Yavuz, T.K. Kim, C.-H. Liu, C. Kuru, C.S. Rustomji, S. Jin, P.R. Bandaru, ACS applied materials & interfaces 7 (2015) 17851-17856.
[13] Y. Xu, W. Bian, W. Jiao, J.H. Tian, R. Yang, Electrochimica Acta 151 (2015) 276-283.
[14] L. Han, P. Tang, Á. Reyes-Carmona, B. Rodríguez-García, M. Torréns, J.R. Morante, J. Arbiol, J.R. Galan-Mascaros, Journal of the American Chemical Society 138 (2016) 16037.
[15] T. Li, Y. Lv, J. Su, Y. Wang, Q. Yang, Y. Zhang, J. Zhou, L. Xu, D. Sun, Y. Tang, Advanced Science 4 (2017) 1700226.
[16] X.-F. Lu, L.-F. Gu, J.-W. Wang, J.-X. Wu, P.-Q. Liao, G.-R. Li, Advanced Materials 29 (2017) 1604437.
[17] W. Bian, Z. Yang, P. Strasser, R. Yang, Journal of Power Sources 250 (2014) 196-203.
[18] X. Ji, S. Hao, F. Qu, J. Liu, G. Du, A.M. Asiri, L. Chen, X. Sun, Nanoscale 9 (2017) 7714-7718.
[19] Y.-F. Xu, X.-D. Wang, H.-Y. Chen, D.-B. Kuang, C.-Y. Su, Advanced Functional Materials 26 (2016) 4414-4421.
[20] C. Singh, A. Goyal, S. Singhal, Nanoscale 6 (2014) 7959-7970.
[21] A.J. Martín, G.O. Larrazábal, J. Pérez-Ramírez, Green Chemistry 17 (2015) 5114-5130.
[22] P.K. Shen, C. Xu, Electrochemistry Communications 8 (2006) 184-188.
[23] G. Chen, Separation & Purification Technology 38 (2004) 11-41.

[24] K. Bouzek, M. Paidar, A. Sadílková, H. Bergmann, Journal of Applied Electrochemistry 31 (2001) 1185-1193.
[25] A. Lambertz, F. Finger, R.E. Schropp, U. Rau, V. Smirnov, Progress in Photovoltaics: Research and Applications 23 (2015) 939-948.
[26] A. Cabot, V.F. Puntes, E. Shevchenko, Y. Yin, L. Balcells, M.A. Marcus, S.M. Hughes, A.P. Alivisatos, Journal of the American Chemical Society 129 (2007) 10358-10360.
[27] A. Cabot, M. Ibáñez, P. Guardia, A.P. Alivisatos, Journal of the American Chemical Society 131 (2009) 11326-11328.
[28] M. Ibáñez, J. Fan, W. Li, D. Cadavid, R. Nafria, A. Carrete, A. Cabot, Chemistry of Materials 23 (2011) 3095-3104.
[29] M. Kruk, M. Jaroniec, S. Guan, S. Inagaki, The Journal of Physical Chemistry B 105 (2001) 681-689.
[30] T. Berestok, P. Guardia, M. Ibáñez, M. Meyns, M. Colombo, M.V. Kovalenko, F. Peiró, A. Cabot, Langmuir 34 (2018) 9167-9174.
[31] T. Berestok, P. Guardia, R. Du, J.B. Portals, M. Colombo, S. Estradé, F. Peiró, S.L. Brock, A. Cabot, ACS Applied Materials & Interfaces 10 (2018) 16041-16048.
[32] Z. Luo, J. Lu, C. Flox, R. Nafria, A. Genç, J. Arbiol, J. Llorca, M. Ibáñez, J.R. Morante, A. Cabot, Journal of Materials Chemistry A 4 (2016) 16706-16713.
[33] S.H. Joo, S.J. Choi, I. Oh, J. Kwak, Z. Liu, O. Terasaki, R. Ryoo, Nature 412 (2001) 169-172.
[34] S. Klaus, Y. Cai, M.W. Louie, L. Trotochaud, A.T. Bell, The Journal of Physical Chemistry C 119 (2015) 7243-7254.
[35] F. Urbain, P. Tang, N.M. Carretero, T. Andreu, J. Arbiol, J.R. Morante, ACS Applied Materials & Interfaces 10 (2018) 43650-43660.
[36] F. Urbain, P. Tang, N.M. Carretero, T. Andreu, L.G. Gerling, C. Voz, J. Arbiol, J.R. Morante, Energy & Environmental Science 10 (2017) 2256-2266.
[37] E. Irtem, T. Andreu, A. Parra, M.D. Hernandez-Alonso, J.R. Morante, Journal of Materials Chemistry A 4 (2016) 10.1039.C1036TA04432H.
[38] M.D.H. ALONSO, G.P. PÉREZ, T. Andreu, E. Irtem, A. Parra, C. Fábrega, J.R. Morante, Filter-press photoelectrochemical water oxidation and CO2 reduction cell, Google Patents, 2018.
[39] F. Urbain, V. Smirnov, J.-P. Becker, A. Lambertz, F. Yang, J. Ziegler, B. Kaiser, W. Jaegermann, U. Rau, F. Finger, Energy & environmental science 9 (2016) 145-154.
[40] C. Trompoukis, A. Abass, J.W. Schüttauf, T. Bosserez, J. Rongé, J. Lauwaert, J.A. Martens, R. Baets, Solar Energy Materials & Solar Cells 182 (2018) 196-203.
[41] M. Qiang, L. Man, L. Pang, X. Ren, C. Li, X. Xu, S.F. Liu, Chemcatchem 8 (2016) 1713-1717.
[42] Y. Tan, H. Wang, P. Liu, Y. Shen, C. Cheng, A. Hirata, T. Fujita, Z. Tang, M. Chen, Energy & Environmental Science 9 (2016) 2257-2261.
[43] N. Jiang, B. You, M. Sheng, Y. Sun, Angewandte Chemie International Edition 54 (2015) 6251-6254.
[44] J. Jia, L.C. Seitz, J.D. Benck, Y. Huo, Y. Chen, J.W.D. Ng, T. Bilir, J.S. Harris, T.F. Jaramillo, Nature Communications 7 (2016) 13237.
[45] F. Urbain, P. Tang, V. Smirnov, K. Welter, T. Andreu, F. Finger, J. Arbiol, J.R. Morante, ChemSusChem 0.
[46] B.M. Klahr, D. Peterson, K. Randolph, E.L. Miller, ECS Transactions 75 (2017) 3-11.
[47] J.H. Montoya, L.C. Seitz, P. Chakthranont, A. Vojvodic, T.F. Jaramillo, J.K. Nørskov, Nature Materials 16 (2016) 70.